Journal of
Nanoelectronics and Optoelectronics
Vol. 16, pp. 1595–1609, 2021
www.aspbs.com/jno

ARTICLE

Technology of Image Motion Compensation for Different Velocity of Aerial Camera Based on Integration Level and Frequency Division Control

Hang Ren[1,4], HanShi Qu[2], TaoTao Hu[3,*], and Xin Wang[1]

When an aircraft is flying sideways, the aerial camera will be in a squint state, and there will be multiple image motions of different sizes on the imaging target at the same time. In this paper, the principle of different velocity image motion in squint imaging of an aircraft is analysed, and the compensation strategy of different velocity image motion is proposed. Then, three methods are used to analyse the adjustment strategy of different velocity image motion compensation, namely, adjusting the integration level of (Time Delayed and Integration) TDICCD, grouping and frequency division control of TDICCD on the image surface, and optimizing the control based on the combination of integration level and frequency division control. Through the simulation analysis, it is concluded that the adjustment of the integration level of TDICCD and the slice grouping control is the optimal method. This method not only ensures the required image SNR of the optical system but also reduces the complex problems of electronic circuit and control system caused by the presence of too many segments and groups. In the actual aerial camera system imaging, this method can be used as an effective method for the compensation for the image motion of different velocity when the aerial camera tilts. Then, the design of the driving circuit and timing generator are described. The validity of the method is verified by indoor simulations and a flight test.

Keywords: Integration Level, Frequency Division Control, Aerial Camera, Image Motion at Different Speeds, TDICCD.

1. INTRODUCTION

To avoid radar surveillance during reconnaissance missions, reconnaissance aircraft often need to fly at high speed and low altitude (high speed to altitude ratio). In this case, image blur will inevitably appear in aerial imaging. The formation of image blur is closely related to the flight attitude of the carrier. Different parameters of the carrier such as flight speed, altitude, roll angle, yaw angle, and pitch angle will produce different image motion patterns. When the aircraft is flying sideways or the lens is pitching to the side for imaging, the aerial camera on the aircraft will be in a squint state. In this case, different positions on the imaging target will have image motions at different speeds, generating complex motion-blurred images, as shown in Figure 1 [1–3].

1.1. Common Image Motion Compensation Methods

The image motion compensation methods developed at present mainly start from three perspectives: First, use electronic means to develop CCD devices with Time Delay and Integration (TDI) functions, and use charge transfer drive technology for specific CCD devices. Controlling the charge transfer speed of the CCD within the integration time can perform image motion compensation; the second is to study the image processing algorithm, through the post-image processing to realize the clarity of the blurred image or correct the image rotation, but the image information will be lost; the third is to use Motion control technology compensates for image shift caused by motion imaging by controlling the inertial stabilization platform, scanning mirror, fast mirror, etc. This method has very

[1]Changchun Institute of Optics, Fine Mechanics and Physics, Chinese Academy of Sciences, Changchun, 130033, China
[2]XiDian University, School of Computer Science and Technology, Xian, 710126, China
[3]School of Physics, Northeast Normal University, Changchun, 130024, China
[4]Key Laboratory of Airborne Optical Imaging and Measurement, Changchun Institute of Optics, Fine Mechanics and Physics, Chinese Academy of Sciences, Changchun, 130033, China
*Author to whom correspondence should be addressed.
Email: hutt262@nenu.edu.cn
Received: 15 December 2021
Accepted: 18 December 2021

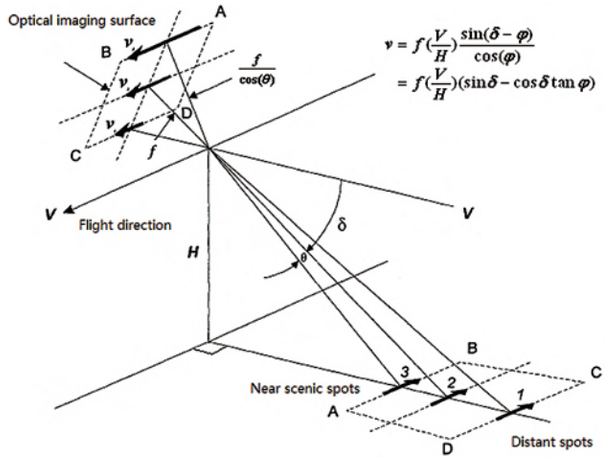

Fig. 1. Schematic diagram of generation of different velocity image motion.

high requirements for structural accuracy, reliability, and stability [4–6].

The Russian National Academy of Sciences has carried out a systematic study on image motion compensation [7, 8]. Researchers represented by BM Mille have proposed two compensation measures for CCD camera imaging compensation: one is optical-mechanical motion compensation, and the other is electronic compensation [9, 10]. And further analyzed the advantages and disadvantages of the two compensation methods, and proved the feasibility of the electronic compensation method [11, 12]. German Aerospace Center Ingo Walter et al. also proposed an image motion compensation scheme for the space CCD imaging system. This scheme uses micromechanical devices, that is, a rotating mirror is set in front of the objective lens, and the space is realized by the rotation of the rotating mirror [13, 14]. The camera optical system performs motion compensation. Japan has also taken some measures to compensate for image motion. In order to interfere with lower loads, scanning imaging using multiple and sweep sampling modes has solved the problem of image motion compensation to a certain extent [15, 16]. In response to the problem of image motion and image shift, Korean scientists have announced that they have designed a set of image motion compensation algorithms, but the feasibility of this compensation algorithm and the compensation effect in practical applications need further verification and analysis [17–18].

The A3 camera is based on acceleration sensor and real-time GPS (Global Position System) data, calculates the required compensation parameters through the encoder data on the instrument, and controls the movement of the image motion compensation mirror in the lens, thereby realizing various displacement changes to the aircraft and the camera platform Image motion compensation caused [19].

The US high-altitude long-endurance UAV-RQ-4 "Global Hawk" UAV photoelectric reconnaissance payload is a typical aerial imaging payload with a large-area fast scanning function. The camera adopts a total reflection optical system and is installed in the inner frame of the two-axis stable frame structure. The two-axis frame with high stability and precision controls the roll and pitch of the camera optical system to achieve the camera's image motion compensation [20].

Taking a squint film stepping frame camera as an example, Zhang Shuqing proposed an image motion compensation scheme that uses a two-axis rotating scanning mirror, combined with a rotating drift mechanism and an exposure curtain slit, and applied geometric optics and spatial analytical geometry knowledge to study the difference. The mechanism of the rapid image movement demonstrates the mathematical relationship between the different speed image movement and the camera depression angle [21, 22]. Xu Yongsen used the method of combining the light vector and the optical axis rotation transformation to establish the light vector and the optical axis unit vector for the translation between the object and the optical axis caused by the flight of the aircraft, and the change of the optical axis direction caused by the attitude change of the aircraft. The relationship between the image shift model of the aerial remote sensor in the squint state is obtained [23, 24]. Zhan Lei et al. used the method of combining the light vector and the optical axis rotation transformation to establish the image movement model of the remote sensor in the squint state, and calculated the forward image movement and the posture image movement of the remote sensor based on the tested working parameters [24]. Wang Lin proposed a method of using the frame to complete the pointing control of the fast mirror to realize the image motion compensation [25]. Chen Weining designed a heading image motion compensation mechanism, and realized the image motion compensation by using a moving target structure [25, 26]. Xiu Jihong proposed a stepping staring system composed of two single-axis fast mirrors and a two-axis frame to compensate for image movement [26, 27]. According to the structure and working principle of the aerial camera lens shutter, Yu Chunfeng established the matrix relationship between the ground object and the image through the coordinate transformation method, that is, to determine the relationship between the shutter exposure time and the image motion value [28–30]. Tian Dapeng proposed a comprehensive image rotation compensation method based on a sliding mode controller with four-channel bilateral control. At the same time, the image translation compensation is performed according to the quantitative relationship between the movement of the scanning mirror and the image translation compensator [31, 32]. Li-zhi et al. established an image point displacement calculation model by using the homogeneous coordinate transformation method,

and accurately introduced common error items such as the axis error of the pendulum mirror to realize image motion compensation [33, 34]. For the image motion compensation of a large field of view space camera., Lubron established an off-axis three-mirror large field of view space camera general image motion velocity field model based on coordinate transformation and attitude dynamics [35, 36]. Wang Zhengxi designed a model reference adaptive controller and proposed an image motion compensation method based on fast mirrors to solve the image motion problem in aerial imaging [37, 38].

1.2. Main Contributions of This Paper

In this paper, the linear TDICCD is spliced into the array CCD, and the TDICCD is controlled by adjusting the integral series and frequency division control to compensate the different velocity image of the aerial camera. In this paper, the principle of different velocity image motion in squint imaging of aircraft is analysed, and the compensation strategy of the different velocity image motion is proposed. Then, three methods are used to analyse the adjustment strategy of the different velocity image motion compensation, namely, adjusting the integration level of TDICCD, grouping and frequency division control of TDICCD on the image surface, and optimizing control based on the combination of the integration level and frequency division control. Using simulation analysis, it is concluded that the optimal method is to adjust the integration level of TDICCD and the slice grouping control. This method not only ensures that the required image SNR of the optical system is achieved but also reduces the complex problems of electronic circuit and control system caused by too many segments and groups. In the actual aerial camera system imaging, this method can be used for effective compensation for the image motion of different velocity when the aerial camera tilts. Then, the design of the driving circuit and timing generator are given. The validity of the method is verified by the indoor simulation and flight test [39, 40].

2. ANALYSIS OF THE ORIGIN OF THE DIFFERENT RATES OF IMAGE MOTION OF THE AIRCRAFT CAMERA AND THE COMPENSATION METHOD

2.1. Analysis of the Origin of the Different Rates of Image Motion of the Aircraft Camera

When the aircraft is tilted, the forward image velocity of the near point target on the image plane is the same as the forward image velocity of the far point target in the single ground area. Thus, the forward image velocity with equal direction and unequal size is defined as the image velocity with different velocity. In addition, the aircraft attitude angle such as the roll angle of the aircraft will also produce the image motion. Next, we will conduct an in-depth study on the origin, size and direction of the image motion. As shown in Figure 1, in the whole array, the image motion rate of the focal plane in the flight direction of the aircraft is not constant. It is determined by the tilt range and the tilt distance r (that is, the distance from the lens to the corresponding point of the ground scene). A larger range corresponds to a smaller image motion rate at the focal plane. Specifically, in the vertical flight direction, the image motion V before the image motion rate of a point is given by Ref. [41]:

$$V_{P2} = \left(\frac{V}{R}\right)\frac{f}{\cos\varepsilon} \tag{1}$$

Here, ε is the half of the field angle, δ is the camera's pitch angle, f is the lens focal length, V is the aircraft's flight speed, and R is the slant distance, that is, the distance from the lens to the point on the focal plane facing the ground. Based on Figure 1, the FPA of the focal plane array can be further described geometrically as follows:

$$\varepsilon = \tan^{-1}\left(\frac{R}{f}\right) \tag{2}$$

Here, for any given ε, y is the distance from a certain point of the ground area taken perpendicular to the flight direction to the centreline. It follows that:

$$R = \frac{H}{\sin(\delta \pm \varepsilon)} \tag{3}$$

where δ is the angle between the centre of the field of view and the horizontal line, and h is the height of the aircraft. Therefore:

$$V_{P2} = f\left(\frac{V}{H}\right)\frac{\sin(\delta \pm \varepsilon)}{\cos\varepsilon} \tag{4}$$

The influence of the image motion in the direction of the focal plane on the image quality can be obtained by calculating the MTF of the image motion of the focal plane array. Based on Formula (4), for a given lens focal length f, pitch angle δ, field angle ε and aircraft velocity height ratio V/h, in the direction perpendicular to the focal plane, the velocity v_y at a point y of the image can be expressed as

$$v_y = f\left(\frac{V}{H}\right)\frac{\sin(\delta + \varepsilon)}{\cos\varepsilon} \tag{5}$$

Calculation and analysis show that the asynchronous image speed is only related to the camera's transverse angle and tilt angle but not to the aircraft's longitudinal angle [42].

When the speed to height ratio of the aircraft decreases, the image motion speed will decrease accordingly. At this time, regardless of how much focal length lens is used to maintain the resolution of the ground image, no improvement in image quality will be obtained. The distance L of the image movement of a point parallel to the flight direction on the focal plane is related to the flight speed V and

the total time t. The total time t is the sum of the exposure time of the focal plane array (that is, the time when the shutter is opened). According to the MTF, the blur degree m of the image is a function of L:

$$M = \frac{\sin(\pi L f_N)}{\pi L f_N} \tag{6}$$

where f_N is the spatial Nyquist frequency which is the highest frequency of interest. Suppose that the flight speed of the carrier to the ground is V, the range of B is 10–50 m/s, the flight height is h, H is either 3000 m or 5000 m, the angle of lens horizontal pitch is δ, the focal length of lens is f, the angle of half field of view of lens is θ, and the speed of the ground far scenic spot is $V_F = f(v_{\text{flight}}/H)\sin(\delta-\varepsilon)/\cos\varepsilon$, and the image moving speed of the ground near scenic spot on the CCD array is $V_N = f(v_{flight}/H)\sin(\delta+\varepsilon)/\cos\varepsilon$. The ratio of the image motion velocity between the near and long-range points is $v_N/v_F = \sin(\delta+\varepsilon)/\sin(\delta-\varepsilon)$. When ε is a fixed value, V_N/V_F increases with the decrease in the elevation angle. For δ in the range of [90°, θ], V_N/V_F is in the range of $[1, +\infty)$. The value range shows that the lateral elevation angle of the lens has a strong influence on the image motion velocity difference between the near and far objects on the CCD plane. With the decrease in δ, the image motion velocity difference cannot be approximated as zero [43].

2.2. Analysis of Compensation for Different Velocity Image Motion of Aerial Camera

In this work, the method of electronic compensation is used to match the image velocity. The process of image motion speed matching is to adjust the line transfer speed of TDICCD to make it consistent with the image motion speed of the reference pixel. The adjustment of the line transfer speed of TDICCD on the image plane can be realized through the adjustment of the charge transfer frequency. Using speed matching, the same target on the ground and the same pixel of the detector can be realized, and the exposure can be superposed [44].

The matching of the image moving speed is realized by adjusting the line frequency of TDICCD, so that the strategy of grouping different speed matching can be used to improve the imaging quality of the edge points of the focal plane when the aerial camera tilts. The focus plane is first grouped, and then the TDICCD in each group is adjusted independently according to the image motion speed of each group's centre point. Theoretically, the distance between the edge of the focal plane and the reference point decreases with increasing number of components, so that a higher MTF is caused by the image moving speed error. However, the TDICCD used in China does not have the function of single-chip frequency division control, that is, the maximum number of packets depends on the number of TDICCDs spliced on the focal plane [45].

The focal plane of the aerial camera studied in this paper is composed of 11 TDICCDs. The effective pixel number of the single TDICCD is 8192, and the pixel size is 10 μM.

2.2.1. Analysis of Different Speed Matching of Different Integral Orders

When the aerial camera performs imaging with a large tilt attitude, the difference in the image moving speed between the edge field of view and the centre field of view is relatively large, and the range of clear imaging can be achieved at this time. To achieve the requirements of full-field imaging with a large attitude angle, it is necessary to consider the problem of alloscopic image motion matching, that is, how to reduce the image motion velocity matching residuals between the non-central field of view pixels and the central field of view pixels [46]. One simple method is to adjust the integration order of TDICCD according to the imaging tilt angle requirement. Of course, when adjusting the integration level of TDICCD, it is necessary to fully consider the influence of the signal-to-noise ratio, lighting conditions and atmospheric conditions of the aerial camera optical system. Figure 2 shows the change of MTF with the swing angle. It is observed from the figure that the maximum tilt angle increases with decreasing TDICCD integration level under the imaging conditions of the system. When different integration levels are selected, the MTF of the vertical integration direction changes little. When the aerial camera is tilted by 40 degrees, the maximum value of the MTF drop in the vertical integration direction of different integration levels is less than 2.5%.

The amount of image motion during integration does not exceed 1/3 of the pixel size, corresponding to a situation where the MTF drop does not exceed 5% and has no significant effect on the imaging quality. As shown

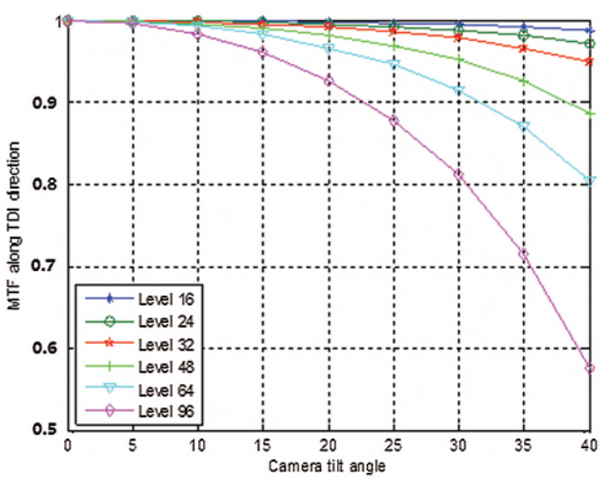

Fig. 2. MTF changes with the tilt angle along TDI in different integration orders.

Table I. Maximum tilt angle of different integration order to meet the imaging conditions.

Points level	96	64	48	32	24	16
Maximum tilt angle	13.6°	20.5°	25.6°	37.2°	43.5°	51.2°

in Table I, using this imaging constraint to evaluate the imaging quality of the system, the maximum tilt angle of the aerial camera that can achieve clear imaging in the full field of view with different integration levels can be obtained.

An examination of Table I shows that a reduction in the integration order of TDICCD can increase the maximum tilt angle of the aerial camera, but the selection of the image area classification order of the camera is related to factors such as the camera's radiation responsivity and ground reflectance. When the position of the aerial camera is fixed, the minimum integration level at this time is determined. Therefore, factors such as lighting conditions and atmospheric conditions become one of the reasons that restrict the aerial camera's large-angle tilt. At the same time, it also shows that reducing the integration level of TDICCD is an effective method to solve the alloscopic image motion matching of the aerial camera. This method is theoretically feasible. However, it faces the problem that the reduction of the TDICCD integration level will greatly reduce the signal-to-noise ratio of the optical system, so that the resulting image may be underexposed, and satisfactory image quality cannot be obtained [47].

2.2.2. Analysis of Different Speed Matching of Different Groups

For the compensation of the allospheric image motion changes, a hierarchical forward motion compensation technique can be used. Some adjacent columns of the focal plane array form a "block." Therefore, the focal plane array consists of many "blocks". During exposure, the charge moves from one pixel to its adjacent pixel along the image motion direction. In the lateral direction (such as across the "block" direction), the charge movement speed varies. Therefore, by synchronizing the movement speed of the charge and controlling the magnitude of the charge image movement speed on the array, the forward image movement compensation can be realized step by step without using any components. Ideally, each column of pixels should have its own rate of vertical charge movement. However, in practice, the focal plane array is divided into a series of "blocks", and the charge movement rate of each block is the average of the velocity of each column in the block.

For the focal plane array of larger pixels, the application of the above method is shown in Figure 3. The pixel information in the array is subdivided into many "blocks". According to the image movement speed at the centre of each block, each block has its own charge movement

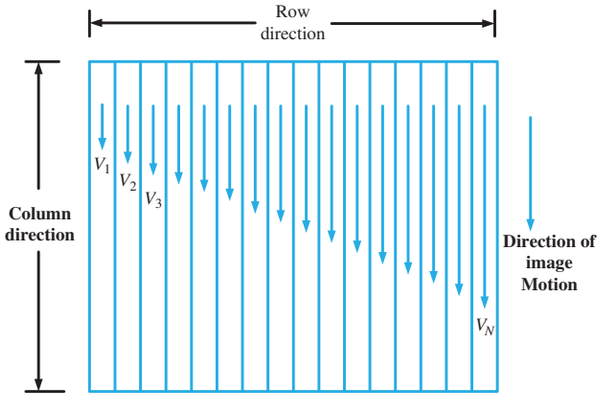

Fig. 3. Schematic diagram of the squint state image segmentation compensation.

rate. The arrows in the figure represent the rate of charge movement. A longer arrow indicates a higher rate. The charge movement rate of the "block" closer to the array edge NADIR is greater, the charge movement rate of the "block" closer to the horizontal line is smaller, and the charge movement rate in the lateral direction of the array changes monotonically. During exposure, when the shutter is open, the charge containing the scene information is collected onto the pixels in the array, and then the charge moves from one pixel to its adjacent pixel according to the charge movement rate of each "block." When the shutter is closed, that is, after the exposure is completed, these accumulated charges containing image information are sequentially read out from the array to the register, one row at a time. The information is then sent to the signal processing device from the register for the user to evaluate. After the signal reading is completed, the array can be used for the next exposure [48].

Expanding Formula (5) and combining with Figure 3, we find that the image motion speed of any point y relative to its edge in the focal plane array is given by:

$$v_y = fl\frac{V}{H}\frac{\sin(\delta+\theta(y-Y/2))}{\cos(\theta(y-Y/2))}\Phi(y-Y/2) + fl\frac{V}{H}\frac{\sin(\delta-\theta(Y/2-y))}{\cos(\theta(Y/2-y))}\Phi(Y/2-y) \quad (7)$$

Here, according to Formula (2), θ varies with the position y, and Φ is a step function defined as $\Phi(y \geq 0) = 1$, $\Phi(y \leq 0) = 0$.

The following formula gives the distance L from any image point to any point y of any image motion compensation area k:

$$L(y,k) = \left\{ v(y) - \sum_i v\left[i\frac{Y}{k} + \frac{Y}{2k}\right] \times \Phi\left(y - \frac{Y}{k}i\right) \times \Phi\left[\frac{Y}{k}(i+1) - y\right] \right\} * t \quad (8)$$

Here, Y is the width of the focal plane, k is the number of the FMC area, and the value of the integer i determines the centre point of the area in the function for which the y value will be subtracted. If the value of $L(y, k)$ is known, then the modulation transfer function MTF of the corresponding array can be calculated by Eq. (6). Since the image motion compensation is carried out step by step, the focal plane array is also divided into individual areas. This method improves the modulation transfer function MTF [49].

We note that here we encounter a problem, namely with an increased number of groups the corresponding control circuit becomes more complicated, and the difficulty of processing subsequent images is also increased. Therefore, the number of groups should be reasonably selected according to image quality requirements. Since 11 TDICCDs are staggered on the substrate in this paper, the number of pixels per TDICCD is 8192. Therefore, this paper proposes four kinds of grouping different speed matching schemes and compares them. The grouping schemes are shown in Figure 4, and the size of the focal plane along the integration direction is ignored here. When divided into one group of different speed matching, the centre of the No. 6 CCD (centre of focal plane) is used as the reference point; when divided into three speed matching groups, the centre of the No. 6 CCD, the splicing point of the No. 2 and No. 3 CCDs, and the No. 9 CCD, are used. The junction with the No. 10 CCD is the reference point; when divided into five groups of allometric matching, the centre of the No. 2, 4, 6, 8, and 10 CCDs (centre of the focal plane) is used as the reference point; when divided into eleven groups of allometric matching To each piece CCD [50–52].

The centre of the CD is the reference point; then the image motion speed of each group of central field of view pixels is used as the reference to calculate the residual error of the edge field of view and the centre field of view of each group, and quantitative analysis of the imaging quality MTF is carried out to determine whether it can meet the requirement of clear imaging in the full field of view of the aerial camera at a large tilt angle. Then, we determine the least grouping strategy that meets the requirements based on the calculation results.

To more clearly and intuitively analyse the impact of the different grouping strategies on image quality, this article uses a more intuitive image quality evaluation method MTF to perform quantitative analysis. According to the relative error of image movement speed matching, the MTF value changes with the swing angle under different grouping strategies, as shown in the Figure 5. Table II shows the MTF with different swing angles corresponding to different grouping strategies under 96-level integration. As seen from the data presented in the table, taking the integration level of 96 as an example, the MTF decreased by 5% as a constraint, the maximum tilt angle of full-field imaging satisfied by different grouping strategies is very different, and as the number of grouping increases the transfer function MTF slows down with the decrease in the swing angle. In the two-component frequency control, the maximum swing angle of the aerial camera for clear imaging in the full field of view is (20°, 25°); in the five-component frequency control, the maximum swing angle of the full-field clear imaging is greater than 40°, meeting the expected large tilt imaging requirements; of course the 11-component frequency control strategy can also meet the requirements of large-tilt imaging, but the control circuit at this time is more than double of that for the five-component frequency, and the 11-group frequency division is used at this time. This strategy is not necessary unless the aerial camera is required to adopt a larger tilt angle to achieve full-field imaging of the image plane [53–54].

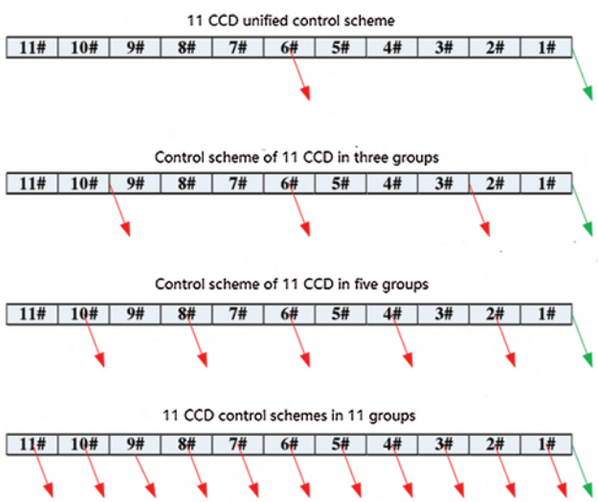

Fig. 4. Group matching scheme.

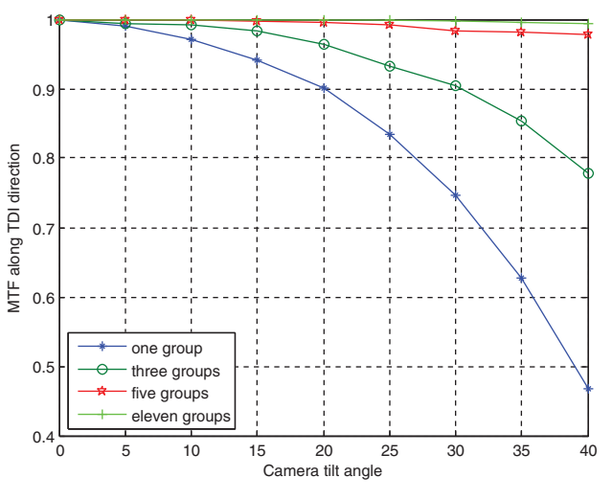

Fig. 5. MTF for different groupings of a 96-level TDICCD varying with tilt angle.

Table II. 96-level integration different grouping strategies corresponding to different tilt angle MTF.

	Swing angle								
MTF	0°	5°	10°	15°	20°	25°	30°	35°	40°
One group	1.0000	0.9912	0.9712	0.9412	0.9011	0.8347	0.7461	0.6267	0.4678
Three groups	1.0000	0.9935	0.9923	0.9831	0.9634	0.9321	0.9045	0.8530	0.7789
Five groups	1.0000	0.9992	0.9990	0.9976	0.9960	0.9921	0.9834	0.9812	0.9776
Eleven groups	1.0000	0.9998	0.9997	0.9995	0.9991	0.9983	0.9971	0.9951	0.9941

Through analysis, it can be concluded that the method of compensating allospheric image motion by frequency-grouping control is feasible, but there are also two problems. The first is that after grouping, different groups of pixels use independent line transfer frequency to control which will make it difficult for each group of pixels to perform image stitching after charge superposition. The difficulty of splicing the output image increases with increasing line transfer frequency difference between the two groups of TDI, so that the splicing can only be realized by identifying and matching the feature points of the image; this increases the difficulty of subsequent image processing. In addition, domestic aerial cameras do not yet have a single-chip crossover control capability, requiring small pieces of the TDICCD for stitching imaging, and then each TDICCD for crossover control. This will also affect the stitching accuracy of the TDICCD. The matching error of the image moving speed has a strong influence on the imaging quality of the system [55–56].

3. AERIAL CAMERA ALLOSCOPIC IMAGE MOTION COMPENSATION TECHNOLOGY BASED ON INTEGRATION OF INTEGRATION LEVEL AND FREQUENCY DIVISION CONTROL

3.1. Compensation and Matching Strategy for Allometric Image Motion

When the aerial camera realizes large-angle tilt imaging, it is difficult to achieve the predetermined imaging quality requirements simply by adjusting the integration order or the frequency division control strategy. Therefore, the integration order can be preferentially adjusted according to the environmental conditions of the imaging position of the aerial camera and combined with the method of frequency grouping to achieve alloscopic image motion matching. We select the appropriate frequency division strategy while adjusting the integration level of TDICCD, which not only considers the requirements of image clarity and contrast but also reduces the difficulty of the subsequent image mosaic matching processing. Because the choice of the integration level affects the signal-to-noise ratio of the system imaging, and the size of the signal-to-noise ratio affects the clarity and contrast of the image, the choice of frequency division strategy directly affects the image quality of the image, and the degradation of the image quality can cause the image to be indistinguishable. Thus, the integration strategy of integration order adjustment and frequency division control can greatly reduce the complexity of the control circuit, and then complete the tilt and clear imaging task.

3.2. Simulation Analysis of Allometric Image Motion Compensation

Figure 6 shows the relationship between MTF and side-swing angle for different integration levels when three-component frequency control is used. It is observed from the figure that to achieve clear imaging of the aerial camera tilted at 30°, it is necessary to first adjust the integration level to 64, and then use three-component frequency control. If the method of reducing the integration order is adopted, the integration order needs to be reduced to 32 to meet the requirements of full-field imaging; if a simple division frequency control strategy is adopted, the image plane TDICCD needs to be divided into five groups for frequency division control [24]. Table III shows the MTF values corresponding to different integration levels of three-component frequency control. An examination of the data presented in the table shows that under three-component frequency control, 48-level integration achieves the maximum side-swing angle under the full-field imaging conditions of the image plane range (35°, 40°), the maximum side swing angle range (30°, 35°) is achieved

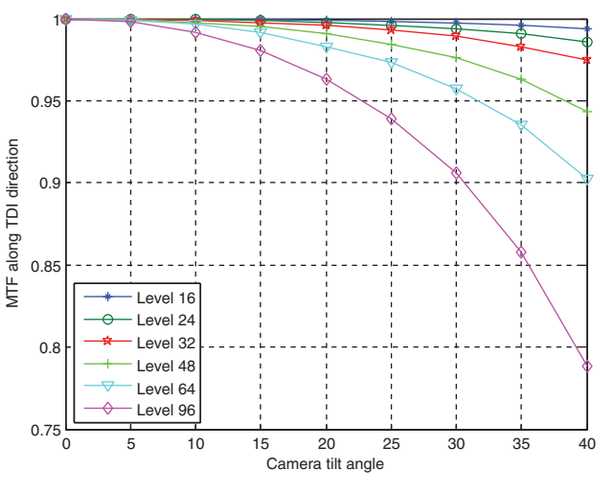

Fig. 6. Three-component frequency control MTF changes with the swing angle.

Table III. MTF with different integration levels corresponding to different swing angles of three component frequencies.

	Swing angle								
MTF	0°	5°	10°	15°	20°	25°	30°	35°	40°
Level 16	1.0000	0.9999	0.9997	0.9995	0.9991	0.9981	0.9971	0.9961	0.9937
Level 24	1.0000	0.9999	0.9994	0.9987	0.9976	0.9961	0.9941	0.9905	0.9856
Level 32	1.0000	0.9998	0.9991	0.9978	0.9960	0.9931	0.9891	0.9831	0.9751
Level 48	1.0000	0.9996	0.9978	0.9952	0.9910	0.9841	0.9761	0.9631	0.9434
Level 64	1.0000	0.9992	0.9965	0.9913	0.9831	0.9732	0.9573	0.9352	0.9024
Level 96	1.0000	0.9982	0.9918	0.9807	0.9631	0.9393	0.9062	0.8581	0.7881

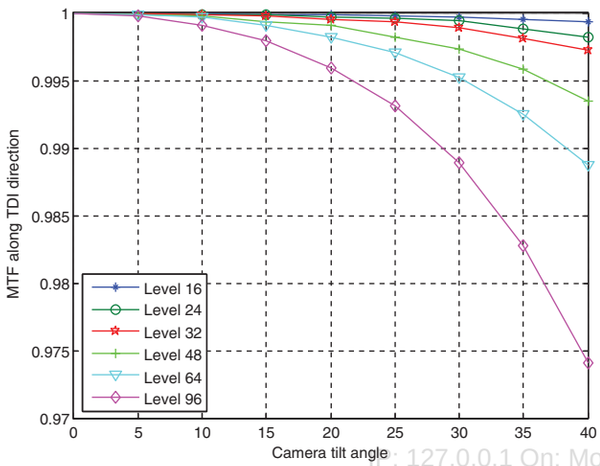

Fig. 7. Five-component frequency control MTF changes with the swing angle.

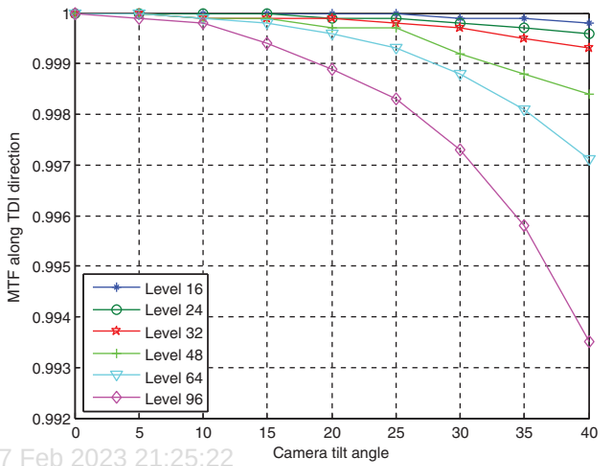

Fig. 8. Eleven-component frequency control MTF changes with tilt angle.

at 64 levels of integration, and the maximum side swing angle range (20°, 25°) achieves at 96 levels of integration.

It is observed from Figure 7 that when five-component frequency control is used, the MTF values corresponding to different integration levels can meet the full-field imaging requirements of the satellite's side-swing 40°. It can be further derived from Table IV that the minimum MTF corresponding to all integration levels when the aerial camera is tilted by 40° is 0.9765, at which time the image motion amount for the entire integration time is less than 1/3 of the pixels. Thus, this method can meet the image quality requirements for all times. We now seek to select the highest integration level to increase the imaging signal-to-noise ratio and improve the imaging quality. If the requirements for image quality are higher, that is, the image motion in the entire integration time is required to be less than 0.2 pixels, and the corresponding MTF should be greater than 0.98 at this time, then when 96-level integration is used, these requirements can be met using the five-component frequency control for the satellite's maximum side swing angle range (35°, 40°).

As shown in Figure 8, when 11-component frequency control is adopted, the full-field image quality requirements can be met when imaging at different integration levels, and the number of grouping groups in this case can be adapted to the imaging requirements of the satellite with a larger side-swing angle. In Table V, the integration level is 96, and the MTF is the minimum value during the

Table IV. Five-component frequency MTF with different integration levels corresponding to different swing angles.

	Swing angle								
MTF	0°	5°	10°	15°	20°	25°	30°	35°	40°
Level 16	1.0000	1.0000	1.0000	0.9999	0.9999	0.9998	0.9997	0.9995	0.9993
Level 24	1.0000	1.0000	0.9999	0.9999	0.9997	0.9996	0.9994	0.9988	0.9982
Level 32	1.0000	1.0000	0.9999	0.9998	0.9995	0.9993	0.9989	0.9981	0.9972
Level 48	1.0000	0.9999	0.9998	0.9993	0.9991	0.9982	0.9973	0.9958	0.9935
Level 64	1.0000	0.9999	0.9997	0.9991	0.9982	0.9971	0.9952	0.9925	0.9887
Level 96	1.0000	0.9998	0.9991	0.9979	0.9959	0.9931	0.9889	0.9828	0.9741

Table V. Eleven component frequency different integration order corresponding to different tilt MTF.

	Swing angle								
MTF	0°	5°	10°	15°	20°	25°	30°	35°	40°
Level 16	1.0000	1.0000	1.0000	1.0000	1.0000	1.0000	0.9999	0.9999	0.9998
Level 24	1.0000	1.0000	1.0000	1.0000	0.9999	0.9999	0.9998	0.9997	0.9996
Level 32	1.0000	1.0000	0.9999	0.9999	0.9999	0.9998	0.9997	0.9995	0.9993
Level 48	1.0000	1.0000	0.9999	0.9999	0.9997	0.9997	0.9992	0.9988	0.9984
Level 64	1.0000	1.0000	0.9999	0.9998	0.9996	0.9993	0.9988	0.9981	0.9971
Level 96	1.0000	0.9999	0.9998	0.9974	0.9989	0.9983	0.9973	0.9858	0.9935

eleven-group frequency control. In this case, the MTF is still above 0.99.

It can be concluded from the above analysis that it is theoretically feasible to compensate the allospheric image motion problem by adjusting the integration order and performing slice and frequency division control. This method integrates and adjusts the advantages of the integration order method and the frequency division method, and not only takes into account the requirements of the imaging illuminance of the camera but also reduces the complexity of the TDICCD drive circuit [25]. The use of this method can solve the problem of alloscopic image motion matching of large field of view and large side-swing imaging, enabling greater ground coverage width of the camera imaging, and thus resolves the contradiction between resolution and coverage width to some extent.

3.3. Design of Sequential Drive Circuit for Allotropic Image Motion

To realize the aviation alloscopic image motion compensation based on the integration of the integration level and frequency division, this section provides an aviation alloscopic image motion compensation CCD drive circuit that supports the integration of the integration level and frequency division. It also includes the CCD, aviation control bus, and system A controller and a signal processing circuit; the aviation control bus, the system controller, the aerodynamic image motion compensation circuit and the signal processing circuit are sequentially connected in communication.

Flight altitude and speed information is provided to the system controller via the aviation control bus. The system controller first stores the received information, and then determines the task parameters based on the information such as the lens focal length, working mode, array size, number of vertical groups in the array, and pixel size. The aerodynamic image motion compensation circuit is used to generate the horizontal driving timing and vertical driving timing required by the CCD and other timings required by the CCD. The horizontal drive circuit is used to amplify and shift the horizontal transfer timing output by the all-speed image motion timing controller, the output amplifier reset pulse and the horizontal pixel combined gate drive clock to drive the CCD; the vertical drive circuit is used to amplify and shift the vertical timing signal output by the fast image motion timing generator to drive the CCD. The signal generated by the CCD is processed by the signal processing circuit and transmitted to the storage and data transmission device.

As shown in Figure 9, the timing generating circuit is used to generate the horizontal driving timing required by the CCD, the vertical driving timing, and other timing required by the CCD. The all-speed image motion timing controller is responsible for forwarding the CCD driving timing generated by the main timing and the image motion compensation driving timing during the all-speed image motion compensation. The vertical drive circuit amplifies the vertical transfer timing to a drive level signal with sufficient voltage and current drive capability, and generates the main DC bias voltage required by the CCD. The horizontal drive circuit horizontal driver amplifies the horizontal transfer timing to the drive that meets the CCD working requirements. The front-end signal processor of the signal processing circuit carries out correlated double sampling, controllable gain amplification, dark level clamping compensation, and analogue-to-digital conversion on the analogue signal output by the CCD. The storage data and transmission device outputs the digital image signal generated by the digital converter from the camera and provides an interface for communication with the host computer.

The timing generator of the shift compensation timing drive circuit can be divided into the following modules, as shown in Figure 10: the bus interface module receives the image motion compensation time interval information from the system controller; the vertical transfer timing selection and distribution module gates the vertical during exposure; the signal generated by the transfer timing and the signal generated by the main timing are gated during the charge output and idle periods; and the phase relationship of each channel is controlled during the distribution process. The horizontal transfer timing distribution module and the signal buffer forwarding module are generated by the forward main timing generation module. The integral order control module is used to generate the timing sequence of TDICCD integral order control, and frequency division control module for generating the driving timing is required to combine TDICCD frequency division.

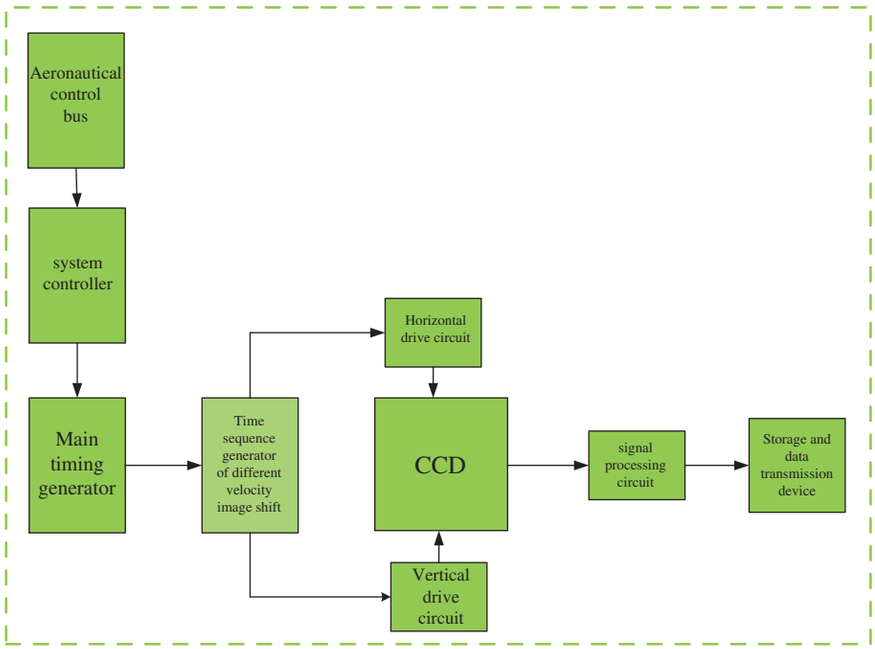

Fig. 9. CCD driving circuit for aeronautical alloscopic image motioning supporting the integration of integration level and frequency division.

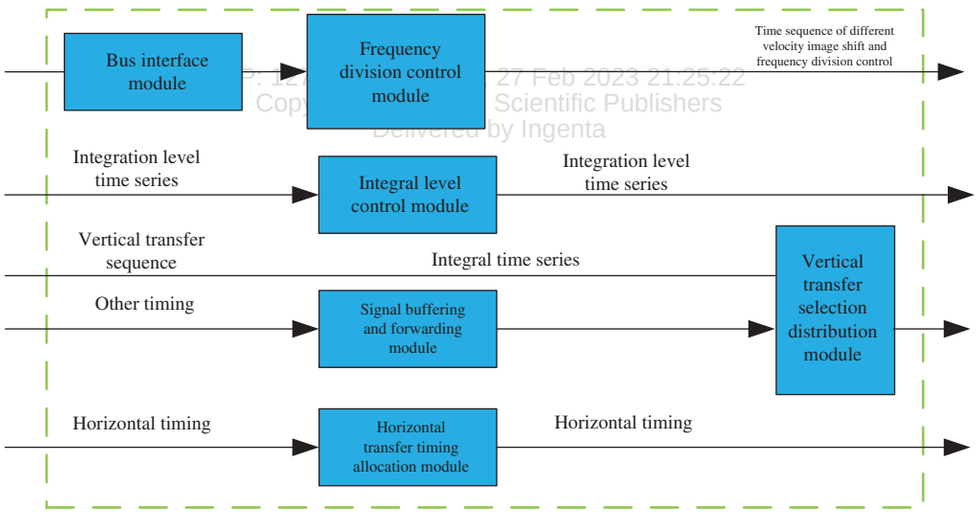

Fig. 10. Design of timing drive generator for allotropic image motion.

4. IMAGE MOTION COMPENSATION IMAGING EXPERIMENT

4.1. Indoor Simulation Experiment

In the aerial imaging systems, flight speed and flight altitude are the main external factors that cause image motion. To simulate the actual motion effect indoors, the test platform was used to obtain images before and after compensation and to evaluate the image clarity.

The focal length of the aerial camera used in the experiment is 180 mm, the tilt angle of the simulated aerial camera is A, and the TDI integration level is 96. The combined TDICCD is divided into 5 groups. The methods used are mechanical image motion compensation method and optical image motion compensation method, the software image motion compensation method, and the electronic image motion compensation method proposed in this paper.

The driving circuit of the CCD is simulated and its photograph is shown in Figure 11. The experimental device consists of a CCD camera, three-axis swing table and PC. As shown in Figure 11, the CCD camera is composed of the designed driving circuit system plus an adjustable lens; the computer is used to control the camera for shooting, to change the rotation speed of the motor and to send the

Fig. 11. Photograph of the experimental verification device.

rotation speed information to the camera; and the computer is installed with the CAMRA link image acquisition card to collect the captured images. The CCD driving circuit is connected to the PC and is operated through the Rs232 interface control. The image acquisition card is responsible for collecting the images, and the camera circuit generates the image motion compensation timing signal. The serial port software is compiled by Microsoft Visual C++ to collect the images, and the data collected from the images are analysed using MATLAB.

The input image is the initial estimate of the point spread function, and the restored image is the final estimate of the function. Through the application function of the blind deconvolution method mentioned above, the software compensation is programmed in MATLAB. The compensation results are shown in Table VI.

Taking letter B as an example, the pixel values of the letter B in the three cases are calculated by importing the images into Envi software, and whether the compensated image motion residual satisfies the requirement of image motion compensation (less than 1/3 pixels) is shown in Table VII.

An examination of the results presented in Table VII shows that the number of image pixels after mechanical compensation is 360 higher than that of the still image, so that the compensation ratio is approximately 1/7. Similarly, the software compensation method adds 438 pixels compared with the still image, thus accounting for approximately 1/6 of the number of pixels in the still image. The optical method compensation method adds 270 pixels, accounting for approximately 1/8 of the number of pixels in the still image. The electronic method compensation method adds 270 pixels, accounting for approximately 1/12.5 of the number of pixels in the still image.

The results for the above four methods indicate that the electronic compensation method is superior to the other compensation methods.

Image quality evaluation is mainly divided into subjective quality evaluation and objective quality evaluation. This paper mainly carries out objective quality evaluation and evaluates the image by calculating the clarity of the image.

Image sharpness refers to the obvious difference in the grey value near the edge of the image or the two sides of the shadow line, that is, the grey change rate is large. Image sharpness represents the relative clarity of the image. Usually, a sharper image is more clear. The definition formula of the image is as follows [31, 32]:

$$GMG = \frac{1}{(M-1)(N-1)} \sum_{i=1}^{M-1} \sum_{j=1}^{N-1} \times \sqrt{\frac{[g(i,j+1)-g(i,j)]^2+[g(i+1,j)-g(i,j)]^2}{2}} \tag{9}$$

where $g(i, j)$ is the grey value of the first row and j column of the image and M and N are the total numbers of the rows and columns of the image, respectively.

Table VI. Comparisons of the results obtained by the software compensation methods.

Target	Stillness	Exercise (uncompensated)	Software (after compensation)	Mechanical method (after compensation)	optical method (after compensation)	Electronic method (after compensation)
Letter					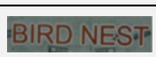	
Torch	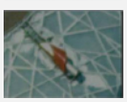	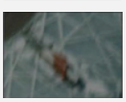			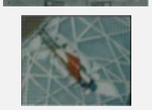	

Table VII. Number of pixels in the CCD target of the image formed by the letter B in Table II (unit: Number).

Target	Stillness	Exercise (uncompensated)	Software (after compensation)	Mechanical method (after compensation)	optical method (after compensation)	Electronic method (after compensation)
Letter	2160	3050	2598	2520	2430	2340
Torch	3125	4341	3891	3692	3521	3214

Table VIII. Image sharpness evaluation results of two compensation methods.

Target	Before compensation	After mechanical method compensation	After software compensation	After optical compensation	After electronic compensation
Letter	1.1713	1.8206	1.9017	1.9213	1.9815
Torch	0.8263	1.6020	1.7121	1.9128	1.9919

In the MATLAB environment, the principle formula is used to calculate the image sharpness. The result of clarity evaluation is as follows.

The comparison results in Table VIII show that the sharpness value after electronic compensation is higher than those of other compensation methods. Therefore, the image after electronic compensation is clearer than those of the other compensation methods.

4.2. Acquire Images from Actual Flight Experiments

Based on the equipment, control procedures and the entire flight experiment flow introduced in the above sections,

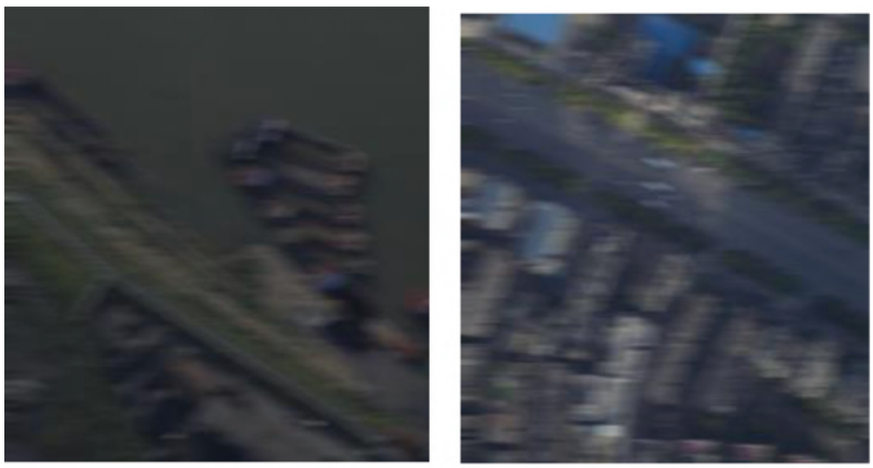

(a) When the shutter is 1/1000, the image before image motion compensation

(b) When the shutter is 1/500, the image before image motion compensation

Fig. 12. Actual flight acquisition image without image motion compensation.

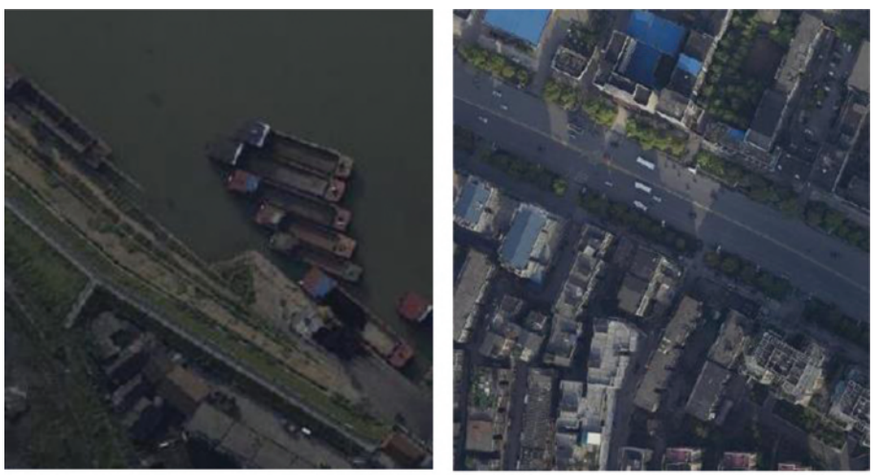

(a) When the shutter is 1/1000, the image after image motion compensation

(b) When the shutter is 1/500, the image after image motion compensation

Fig. 13. Actual flight acquisition image with image motion compensation.

a flight experiment was conducted in the urban area of HuaYin. During the flight experiment, for the different shutter speeds, the two images without image motion compensation and with image motion compensation were shot separately, as described below. When the shutter is set to 1/1000 and 1/500, the image examples without image motion compensation are shown in Figures 12(a) and (b), and sample images after image motion compensation are shown in Figures 13(a) and (b).

5. CONCLUSION

For allospheric image motion when the aerial camera is tilted, an allospheric image motion compensation strategy is proposed. We do use three methods to achieve the matching of allospheric image motioning speeds. The analysis of the advantages and disadvantages of the three methods proves that the method of the integral order adjustment and component frequency control compensation is the most effective method of allometric image motion compensation; this method combines and adjusts the advantages of the integral order method and the component frequency method, taking into account the agile satellite camera imaging. The requirement of illuminance reduces the complexity of TDICCD drive circuit. The use of this method can solve the problem of alloscopic image motion matching of a large field of view and large side swing imaging. Then, the design of the driving circuit and timing generator are given. The validity of the method is verified by indoor simulations and a flight test. The effectiveness of the method is verified.

Conflicts of Interest

The authors declare no conflict of interest.

Acknowledgments: This work was supported by the National Natural Science Foundation of China (Grant No. 62175233).

References and Notes

1. Lareau, A.G., Beran, S.R., Lund, J.A. and Pfister, W.R. **1992**. Electro-Optical Imaging Array with Motion Compensation. U.S. Patent 5,155,597, p.13.
2. Janschek, K. and Tchemykh, V. **2001**. Optical Correlator for Image Motion Compensation in the Focal Plane of a Satellite Camera. *Proceedings of the 15th IFAC Symposium on Automatic Control in Aerospace*, September 2–7; Bologna, Italy, pp.378–382.
3. Olson, G.G., **2002**. Image motion compensation with frame transfer CCDs. *Proc. SPIE*, Vol. 4567, pp.153–160.
4. Bosiers, J.T., Kleimann, A.C., van Kuijk, H.C., Le Cam, L., Peek, H.L., Maas, J.P. and Theuwissen, A.J., **2002**. Frame transfer CCDs for digital still cameras: Concept, design, and evaluation. *IEEE Trans. Electron. Devices*, *49*, pp.377–386.
5. Hussain, R., Noyan, M.A., Woyessa, G., Retamal Marín, R.R., Martinez, P.A., Mahdi, F.M., Finazzi, V., Hazlehurst, T.A., Hunter, T.N., Coll, T., Stintz, M., Muller, F.,Chalkias, G. and Pruneri, V., **2020**. An ultra-compact particle size analyser using a CMOS image sensor and machine learning. *Light Sci. Appl.*, *9*(21), DOI: 10.1038/s41377-020-0255-6.
6. Li, D.-Y., Xia, Q., Yu, T.-T., Zhu, J.-T. and Zhu, D., **2021**. Transmissive-detected laser speckle contrast imaging for blood flow monitoring in thick tissue: From monte carlo simulation to experimental demonstration. *Light Sci. Appl.*, *10*(241), DOI: 10.1038/s41377-021-00682-8.
7. Gach, J.L., Darson, D., Guillaume, C., Goillandeau, M., Cavadore, C., Balard, P., Boissin, O. and Boulesteix, J., **2003**. A new digital CCD readout technique for ultra-low-noise CCDs. *Astronom. Soc. Pac.*, *115*, pp.1068–1071.
8. Markelov, S.V., Murzin, V.A., Borisenko, A.N., Ivaschenko, N.G., Afanasieva, I.V. and Ardilanov, V.I., **2000**. A high-sensitivity CCD camera system for observations of early universe objects. *Astonom. Astrophys. Trans.*, *19*, pp.579–583.
9. Papaioannou, M., Plum, E., Rogers, E.T. and Zheludev, N.I., **2018**. All-optical dynamic focusing of light via coherent absorption in a plasmonic metasurface. *Light Sci. Appl., 7*, p.17157. DOI: 10.1038/lsa.2017.157.
10. Gach, J.L., Darson, D., Guillaume, C., Goillandeau, M., Boissin, O., Boulesteix, J. and Cavadore, C., **2004**. *Zero Noise CCD: A New Readout Technique*. Science Detectors for Astronomy, Springer, Dordrecht, The Netherlands, pp.603–610.
11. Wu, S., Cheng-Shan, H., Heng-Yi, L., Xu-Cheng, X. and Chang-Hong, H., **2019**. Dynamic range extending method for push-broom multispectral remote sensing cameras. *Chinese Optics*, *12*(4), pp.905–912.
12. Smith, S.L., Mooney, J., Tantalo, T.A. and Fiete, R.D., **1999**. Understanding image quality losses due to smear in high-resolutionremote sensing imaging systems. *Optical Engineering*, *38*(5), pp.821–826.
13. Miller, B.M. and Rubinovich, E.Y., **2007**. Image motion compensation at charge-coupled device photographing in delay-integration mode. *Automation and Remote Control*, *68*(3), pp.564–571.
14. Hu, H., Lin, X., Wong, L.J., Yang, Q., Liu, D., Zhang, B. and Luo, Y., **2022**. Surface Dyakonov-Cherenkov radiation. *eLight, 2*, p.2, DOI: 10.1186/s43593-021-00009-5.
15. Bremer, J.C. and Barnes, W.L., **1999**. Seanning Technique for Advanced Geosynchronous Studies Imager: Conical Scanning to Compensate for Image Rotation. *Proceedings of SPIE—The International Society for Optical Engineering*, Vol. 3750, pp.35–46.
16. Avola, D., Cinque, L., Fagioli, A., Foresti, G.L. and Piciarelli, C., **2021**. Automatic estimation of optimal UAV flight parameters for real-time wide areas monitoring. *Multimed. Tools Appl.*, *80*, pp.25009–25031.
17. Vallapureddy, S.R., Banyal, R.K., Rengaswamy, S., Kamath, P.U. and Selvaraj, A., **2020**. Development of image motion compensation system for 1.3 m telescope at vainu bappu observatory. *Research in Astronomy and Astrophysics, 20*(1), p.12.
18. Ustun, D., **2020**. An enhanced adaptive butterfly optimization algorithm rigorously verified on engineering problems and implemented to ISAR image motion compensation. *Engineering Computations, 37*(9), pp.3543–3566.
19. Ramachandran, M., Agarwal, M.K. and Daniel, D.A., **2020**. Efficient on board image motion compensation for orbital inclination and eccentricity of geostationary weather satellites. *Proceedings of the Institution of Mechanical Engineers Part G Journal of Aerospace Engineering*, DOI: 10.1177/0954410019900706.
20. Holst, G.C., **1998**. *CCD Arrays, Cameras, and Displays*, 2nd edition, USA, JCD Publishing, Willmann-Bell.

21. Zhang, S., Zhang, Y., Zhou, C. and Wang, Z., **2014**. Image motion model of azimuthally photography for satellite borne TDICCD camera. *Infrared and Laser Engineering*, *43*(6), pp.1823–1829.

22. Zhang, S. and Li, T., **2014**. Analysis on different rates image motion of space camera with a scanning mirror. *Acta Optica Sinica*, *34*(2), p.0228006 (in chinese).

23. Yong-Sen, X., Ya-Lin, D., Hai-Ying, T. and Bin, D., **2007**. Calculation and compensation for image motion of aerial remote sensor in oblique situation. *Optics and Precision Engineering*, *15*(11), pp.1779–1783.

24. Lei, Z., Ya-Lin, D., Hong-Wen, Z. and Hu, L., **2009**. Methods and theories analysis of image motion compensation based on LOROP cameras. *Laser & Infrared, 39*(4), pp.423–426.

25. Tang, R., Fritsch, D., Cramer, M. and Schneider, W., **2012**. A flexible mathematical method for camera calibration in digital aerial photogrammetry. *Photogrammetric Engineering and Remote Sensing*, *78*(10), pp.1069–1077.

26. Wang, L., Liu, X. and Wang, C., **2019**. Modeling and design of fast steering mirror in image motion compensation for backscanning step and stare imaging systems. *Optical Engineering, 58*(10), p.1.

27. Chen, W., Lei, Y. and Yang, H., **2019**. Research on the Fast Image Motion Compensation Technology of Aerial Digital Camera. *The 2nd International Conference*, pp.71–74. DOI: 10.1145/3341016.3341641.

28. Chun-Feng, Y., Zhi-Chao, C., Ping, J., Nai-Xiang, W. and Han, H., **2020**. Analysis of the effect of lens shutter on image motion in aerial camera. *Chinese Optics*, *13*(3), pp.616–626.

29. Xiu, J., Huang, P., Li, J., Zhang, H. and Li, Y., **2020**. Line of sight and image motion compensation for step and stare imaging system. *Applied Sciences*, *10*(20), p.7119.

30. Tian, D., Wang, Y., Wang, Z., Wang, F. and Gao, H., **2019**. Long integral time continuous panorama scanning imaging based on bilateral control with image motion compensation. *Remote Sensing*, *11*, p.1924.

31. Wang, D.J., Zhang, T. and Kuang, H.P., **2011**. Clocking smearing analysis and reduction for multi phase TDI CCD in remote sensing system. *Optics Express*, *19*(6), pp.4868–4880.

32. Li-Zhi, X., Yi, L. and Zhi-Yuan, G., **2019**. Image motion calculation and error distribution for aerial whisk-broom imaging. *Optics and Precision Engineering*, *27*(10), pp.2071–2079.

33. Peng-Luo, L., Yong-Chang, L., Long-Xu, J., Guo-Ning, L., Yi-Nan, W. and Wen-Hua, W., **2016**. Image motion velocity field model of space camera with large field and analysis on three-axis attitude stability of satellite. *Optics and Precision Engineering*, *24*(9), pp.2173–2182.

34. Shao-Xin, W., Ke-Qi, Q., Yu-Kun, W., Zhi, W. and Li-Heng, C., **2019**. Study on loss of performance in inertial sensors due to electrode asymmetry. *Chinese Optics*, *12*(3), pp.455–462.

35. Jian-Rong, W., Ren-Xiang, W. and Xin, H., **2019**. On-orbit calibration of camera parameters based on line-matrix charge-coupled device imagery. *Optics and Precision Engineering*, *27*(4), pp.984–989.

36. Zheng-Xi, W., Bao, Z., Xian-Tao, L. and Shi-Tao, Z., **2020**. Application of fast steering mirror in image motion compensation. *Chinese Optics*, *13*(1), pp.95–105.

37. Yu, C.-F., Chen, Z.-C., Jia, P., Wang, N.-X. and Hou, H., **2020**. Analysis of the effect of lens shutter on image motion in aerial camera. *Chinese Optics, 13*(3), pp.616–626.

38. Li-Zhi, X., Chang-Xiang, Y., Yi, L. and Zhi-Yuan, G., **2019**. Image motion calculation and error distribution foraerial whisk-broom imaging. *Optics and Precision Engineering*, *27*(10), pp.2071–2079.

39. Peng, L., Bo, C., Ya-Chao, Z., Ling-Ping, H. and Xiao-Dong, W., **2019**. Imaging quality evaluation of soft X-ray grazing incidence telescope. *Optics and Precision Engineering*, *27*(10), pp.2136–2143.

40. Kisoo, K., Kyung-Won, J., Jae-Kwan, R. and Ki-Hun, J., **2020**. Biologically inspired ultrathin arrayed camera for high-contrast and high-resolution imaging. *Light Sci. Appl.*, *9*(28), DOI: 10.1038/s41377-020-0261-8.

41. Cheng-Hao, L., Xu, J., Qi, H.E., Xiao-Hui, Z. and Ning, L.I., **2020**. Design of high spatial and temporal resolution dynamic star simulator. *Optics and Precision Engineering, 28*(3), pp.515–525.

42. Wang, D., Liu, F., Liu, T., Sun, S.L., He,Q. and Zhou, L., **2021**. Efficient generation of complex vectorial optical fields with metasurfaces. *Light Sci. Appl.*, *10*, p.67. DOI: 10.1038/s41377-021-00504-x.

43. Xiong, J. and Wu, S.T., **2021**. Planar liquid crystal polarization optics for augmented reality and virtual reality: From fundamentals to applications. *eLight*, *1*, p.3. DOI: 10.1038/s41377-021-00567-w.

44. Li, C., Wang, H., Wang, F., Li, T., Xu, M., Wang, H., Wang, Z., Zhan, X., Hu, W. and Shen, L. **2020**. Ultrafast and broadband photodetectors based on a perovskite/organic bulk heterojunction for large-dynamic-range imaging. *Light Sci. Appl.*, *9*, p.31. DOI: 10.1038/s41377-020-0264-5.

45. Chang, X., Bian, L. and Zhang, J., **2021**. Large-scale phase retrieval. *eLight*, *1*, p.4, DOI: 10.1038/s41377-020-0264-5.

46. Wu, S., Cheng-Shan, H., Heng-Yi, L., Xu-Cheng, X. and Chang-Hong, H., **2019**. Dynamic range extending method for push-broom multispectral remote sensing cameras. *Chinese Optics*, *12*(4), pp.905–912.

47. Jin, Z., Janoschka, D., Deng, J., Ge, L., Dreher, P., Frank, B., Hu, G., Ni, J., Yang, Y., Li, J., Yu, C., Lei, D., Li, G., Xiao, S., Mei, S., Giessen, H., Heringdorf, F.M.Z. and Qiu, C.-W., **2021**. Phyllotaxis-inspired nanosieves with multiplexed orbital angular momentum. *eLight*, *1*, p.5, DOI: 10.1186/s43593-021-00005-9.

48. Zhao, Y., Song, B., Wang, M., Zhao, Y. and Fan, Y., **2021**. Halftone spatial frequency domain imaging enables kilohertz high-speed label-free non-contact quantitative mapping of optical properties for strongly turbid media. *Light Sci. Appl.*, *10*, p.245, DOI: 10.1038/s41377-021-00681-9.

49. Qi, P., Luo, Y., Shi, B., Li, W., Liu, D., Zheng, L., Liu, Z., Hou, Y. and Fangl, Z., **2021**. Phonon scattering and exciton localization: Molding exciton flux in two dimensional disorder energy landscape. *eLight*, *1*, p.6, DOI: 10.1186/s43593-021-00006-8.

50. Cheng-Hao, L.I., Xu, H.E., Qi, J.I., Xiao-Hui, Z. and Ning, L.I., **2020**. Design of high spatiotemporal resolution dynamic star simulator. *Optics and Precision Engineering*, *28*(3), pp.515–525.

51. Chen, Z. and Segev, M. **2021**. Highlighting photonics: Looking into the next decade. *eLight*, *1*, p.2, DOI: 10.1186/s43593-021-00002-y.

52. Rank, E.A., Sentosa, R., Harper, D.J., Salas, M., Gaugutz, A., Seyringer, D., Nevlacsil, S., Maese-Novo, A., Eggeling, M., Muellner, P., Hainberger, R., Sagmeister, M., Kraft, J., Leitgeb, R.A. and Drexler, W., **2021**. Toward optical coherence tomography on a chip: In vivo three-dimensional human retinal imaging using photonic integrated circuit-based arrayed waveguide gratings. *Light Sci. Appl.*, *10*(6), DOI: 10.1038/s41377-020-00450-0.

53. Zhang, B.Y., Kong, D.Z., Liu, J.G., Wu, X.X. and Dong, D.Y., **2020**. Compensation of star image motion for a CMOS image sensor with a rolling shutter. *Chinese Optics, 13*(6), pp.1276–1284. DOI: 10.37188/CO.2020-0089.

54. Yang, W., Wenjie, Z., Lin, W., Xuemin, L., Meng, F. and Shirui, P., **2016**. Iterative views agreement: An iterative low-rank based structured optimization method to multi-view spectral clustering. *AAAI Press*, arXiv:1608.05560.

55. Wang, Y., Wu, L., Lin, X. and Gao, J., **2018**. Multi-view spectral clustering via structured low-rank matrix factorization. *IEEE Trans. Neural Networks Learn. Syst.*, *29*, pp.4833–4843.

56. Stoev, I.D., Seelbinder, B., Erben, E., Maghelli, N. and Kreysing, M., **2021**. Highly sensitive force measurements in an optically generated, harmonic hydrodynamic trap. *eLight*, *1*, p.7, DOI: 10.1186/s43593-021-00007-7.